JOURNAL OF MAGNETIC RESONANCE **134,** 280–286 (1998)
ARTICLE NO. MN981495

Fourier Reconstruction as a Valid Alternative to Filtered Back Projection in Iterative Applications: Implementation of Fourier Spectral Spatial EPR Imaging

G. Placidi,[1] M. Alecci, S. Colacicchi, and A. Sotgiu

INFM, c/o Dipartimento di Scienze e Tecnologie Biomediche, Universitá dell'Aquila, Via Vetoio 10, 67010 L'Aquila, Italy

Received August 5, 1997; revised April 13, 1998

The qualitative equivalence between the Fourier reconstruction (FR) algorithm and the filtered back projection (FBP) algorithm is demonstrated when all the different phase errors that can occur in FR are eliminated. The causes of phase errors are underlined and methods to eliminate them are presented. The practical comparison between FR and FBP has been evaluated on a numerical test image and the results are reported, demonstrating the qualitative equivalence. FR has the advantage of being very computationally efficient. In fact, the time spent to obtain the FR image was 1/20 of that used to obtain the FBP image. Because of the computational efficiency of FR and the good quality of the results obtained, an iterative version of FR has been used to implement the spectral–spatial imaging (SSI) algorithm in the field of electron paramagnetic resonance imaging (EPRI). An experimental example, demonstrating its good performance, is reported. **© 1998 Academic Press**

INTRODUCTION

Imaging from projections requires the application of a reconstruction algorithm (*1–3*). The numerical reconstruction techniques used for this purpose can be grouped into two basic classes: one in which the reconstruction is performed in the signal space, and one in which it is performed in Fourier space.

Among the methods performed in signal space is filtered back projection (FBP). Fourier reconstruction (FR) is the most important method operating in Fourier space. It has been shown that there is a complete theoretical equivalence between FBP and FR (*1, 3*). In fact, both are interpreted by means of a straightforward and interesting theorem referred to as the projection-slice theorem (*1*). For this reason, both the algorithms belong to the group of so-called analytical algorithms.

The differences between these are of an operative kind and arise from the behavior of the algorithms while finding an approximate solution to the problem. The solution is necessarily an approximation because of the limited number of projections, the limited number of sample points for each projection, and the noise that affects the measured data.

FBP is used in a large number of applications (*4–8*), although it is much slower than FR, which exploits the quickness of the fast Fourier transform algorithm (*9*). The reason is that FR is more sensitive to errors in calculation that can occur in Fourier space: an error in Fourier space, in fact, will be reflected on the whole image. The most serious effect could be the introduction of phase errors on the image that imply the loss of the Hermitian condition of its Fourier transform (supposing that the unknown image is a real function). In this case, the reconstructed image is a complex function and the calculation of its modulus is the only way to collect information, both from the real and the imaginary parts. Zones in which the image assumes negative values (i.e., less than zero), which we refer to as negative information, are thus completely lost and the algorithm fails when this information assumes a physical relevance. In many applications, negative values have no physical relevance, and it is useful to apply the nonnegativity constraint to improve the reconstruction quality. But, if we are forced to use the modulus representation, it is impossible to distinguish and eliminate erroneous negative information produced by the reconstruction technique. This limitation hinders the use of an iterative version of FR when treating very noisy data or missing-angle applications (*4*). In many areas, in which reconstruction from projections is required, these conditions frequently exist and FBP is commonly used instead.

Starting from the assumption of the theoretical equivalence of the two methods, we show that, when all types of phase errors are eliminated, FR performs as well as FBP, even in the presence of negative information. The practical comparison will be assessed by a numerical test image, showing the qualitative equivalence of the results. An iterative version of FR has been used to implement the spectral–spatial imaging (SSI) algorithm in the field of electron paramagnetic resonance imaging (EPRI) (*4, 5*).

The FR algorithm has been applied to reconstruct two-dimensional (2D) images, from a set of one-dimensional (1D) projections. Three-dimensional (3D) reconstruction is a natural

[1] To whom all correspondence should be addressed. E-mail address: Placidi@fismedw2.univaq.it.

1090-7807/98 $25.00
Copyright © 1998 by Academic Press
All rights of reproduction in any form reserved.

extension of the 2D case (*10–12*). The algorithm has been implemented using Matlab on a Pentium IBM-compatible computer.

FOURIER RECONSTRUCTION TECHNIQUE

Let $f(x, y)$ be a 2D function that represents the unknown image. The integral of $f(x, y)$ through a line s perpendicular to a direction ϕ on the sample is called the ray sum. The whole set of ray sums perpendicular to that direction constitutes the projection (*1, 13*) of the image at the ϕ angle, i.e.,

$$p_\phi(r) = \int_{-\infty}^{\infty} f(r, s)ds, \qquad [1]$$

where $r = x \cos \phi + y \sin \phi$ and $s = x \sin \phi - y \cos \phi$.

For each projection $p_\phi(r)$ collected in the space domain, the 1D FT is given by

$$P_\phi(\omega) = \int_{-\infty}^{\infty} p_\phi(r)e^{i\omega r}dr, \qquad [2]$$

where $\phi = \tan^{-1}(\omega_2/\omega_1)$ and $\omega = (\omega_1^2 + \omega_2^2)^{1/2}$.

The image $f(x, y)$ can be calculated by 2D inverse Fourier transform,

$$f(x, y) = \int_{-\infty}^{\infty}\int_{-\infty}^{\infty} F(\omega_1, \omega_2)e^{-i(\omega_1 x+\omega_2 y)}d\omega_1 d\omega_2, \qquad [3]$$

in which the coefficients $F(\omega_1, \omega_2)$ are evaluated using new axes (r, s) rotated by an angle ϕ with respect to the positive x-axis,

$$F(\omega_1, \omega_2) = \int_{-\infty}^{\infty}\int_{-\infty}^{\infty} f(r, s)e^{i\omega r}drds, \qquad [4]$$

and ω is defined as before.

By changing the order of integration, we see that the s-integral is the projection $p_\phi(r)$, as given in [1], so that

$$F(\omega, \phi) = F(\omega_1, \omega_2) = \int_{-\infty}^{\infty} p_\phi(r)e^{i\omega r}dr = P_\phi(\omega), \qquad [5]$$

where $F(\omega, \phi)$ represents the FT of $f(x, y)$ in polar coordinates in the frequency domain. Equation [5], known as the projection-slice theorem (*14*), states that each Fourier coefficient of the density function is equal to the corresponding Fourier coefficient of the projection taken at the same angle. This equation gives a direct operative method in order to derive a reconstruction algorithm, called Fourier reconstruction (FR), that operates as follows:

(a) It creates the one-dimensional Fourier transform of each projection.

(b) It places each 1D Fourier Transform on a 2D plane at the proper angle and position.

(c) It uses the inverse 2D Fourier transform to obtain the image.

In general, the exact reconstruction of the image $f(x, y)$, by using Eq. [3], requires an infinite number of projections. Moreover, we are supposing that $P_\phi(\omega)$ is a continuous function. But, in experimental conditions, a finite number L of projections is collected in polar coordinates, at angular increments $\Delta\phi_j$. Moreover, for each projection N data points are acquired with spatial increments Δr. In this case, the FR image can be approximated by

$$f(x, y) \approx \sum_{k=-N/2}^{N/2}\sum_{J=-N/2}^{N/2} F(\omega_k, \omega_j)e^{-i(\omega_k x+\omega_j y)}\Delta\omega_k\Delta\omega_j, \qquad [6]$$

and the 1D Fourier transform of $p_\phi(r)$ has the form

$$P_\phi(\omega) \approx \sum_{k=-N/2}^{N/2} p_\phi(r_k)e^{i\omega r_k}\Delta r_k. \qquad [7]$$

In these conditions, the FR algorithm has to be changed, adding a new step, between (b) and (c), to include an interpolation process in order to obtain a two-dimensional Cartesian grid of Fourier coefficients.

During the implementation of this algorithm, two types of errors can occur. One is strongly dependent on the accuracy of the interpolation technique, on the number of projections, and on the sampling interval of each projection. This type influences the image quality, but does not eliminate any intrinsic characteristic of the image, such as being a real function. Moreover, it has been demonstrated elsewhere (*13, 14*) that these sorts of errors can be easily reduced by using more accurate interpolation techniques.

The second type, the so called phase errors, is specific to FR and can occur for different reasons, violating the Hermite condition. In fact, phase errors are generated if not all of the Fourier coefficients are correctly positioned in ω-space, or when their value is not correctly evaluated both for the real and imaginary parts. Moreover, the condition that must hold is that the zero-frequency (DC component) of each projection must be placed at the same point at which the 2D Fourier transform places the zero frequency of an image of the same dimensions. This placement is strongly dependent on the implementation of the FT algorithm and, when treating an $N*N$ image, N being an

even number, the FT algorithm could place the zero frequency at one of four points: $(N/2, N/2)$, $(N/2 + 1, N/2)$, $(N/2, N/2 + 1)$ or $(N/2 + 1, N/2 + 1)$, because the logical center of the image does not correspond to a physical one. If this correspondence is violated, phase errors can occur that transfer relevant information to the imaginary part of the image. The central point of the Fourier transform of the projections must be at exactly the same position where the Fourier transform algorithm would place the DC point.

NUMERICAL EXPERIMENT

The experiment reported in this section is intended to show that FR can produce large phase errors in the reconstructed image. However, it will show the practical equivalence between FR and FBP, once any sort of error in FR has been eliminated.

For this purpose, the two techniques have been tested using calculated data obtained by a two-level image, composed of an "F" printed on a white circle (see Fig. 1A). A set of 128 projections, each sampled on 128 points, have been numerically calculated (without adding noise) to reconstruct 128*128 images. The images reconstructed by FR and FBP are shown in Figs. 1B and 1C, respectively. Figure 2A shows the real part and Fig. 2B the imaginary part of the image reconstructed by FR, presenting phase errors due to only a one-point frequency shift in the positioning of the Fourier coefficients of one projection. The Hermite condition of the Fourier transform of the image is violated.

The resulting image will be complex, and a consistent part of it has been shifted to its imaginary part. In this condition, the only possibility of using the information contained in the real and imaginary parts is by taking the modulus of the image. This results in the loss of the negative information in the image. When the nonnegativity constraint ($f(x, y) > 0$) holds, the modulus does not allow the zeroing of the points (x, y) in which $f(x, y) < 0$, these being errors caused by the approximation processes.

However, when FR uses correct positions for the Fourier coefficients and ensures a correct interpolation process, it is possible to obtain an image containing all the meaningful data in its real part (see Fig. 2C, the same as Fig. 1A). In this case, its imaginary part will be almost everywhere zero (see Fig. 2D) and will show very few spurious values which are the residual effects of numerical calculation errors intrinsic to the fast Fourier transform algorithm (these values are of the order of 10^{-25} and the image values are between zero and one). In this case, it is possible to use the nonnegativity constraint to eliminate spurious negative oscillations (due to missing angle or sampling), improving the image quality.

The comparison between Figs. 1B and 1C suggests the following considerations:

1. The images are very similar and this fact is also demonstrated by the values of the mean squared errors (MSE) defined as in Ref. *15* ($MSE_{FR} = 0.005$, $MSE_{FBP} = 0.008$).
2. The nonnegativity constraint can be used in each method.
3. The FR image has been obtained in 2 minutes; the FBP image has been obtained in 40 minutes.

The large difference in computational performance is due to the different operational behavior of the two methods. In fact, if N is the number of projections used, the computational complexity of FR grows as $N^2 \log_2 N$, having supposed that the number of projections is of the same order as the number of the sampling points of each projection and of the image (*1*). The computational complexity function of FBP, in the same conditions, grows as N^3. As an example, if we place $N = 128$, FR will be about 18 times more computationally efficient than FBP. It is important to emphasize that if N is not a power of 2, both algorithms have computational complexity that grows as N^3. In fact, FR uses the advantages of the FFT algorithm that grows as $N \log_2 N$ if N is a power of 2, and N^2 otherwise (*1*).

The comparison has been done on the assumption that interpolation errors are correctly treated and minimized. To make the possibility of these errors negligible, we have used a greater number of projections than necessary.

EXPERIMENTAL EPR APPLICATION: SPECTRAL–SPATIAL IMAGING

The operative comparison between the two results has shown the qualitative equivalence of the two methods, starting from the effective advantage of FR with respect to FBP in computational performance. We can now show, as an example, the use of an iterative version of FR in an important application of EPRI that uses missing angle reconstruction: SSI (*4, 5*).

In EPR spatial imaging, the goal is to map the spin density distribution of an unknown object from a set of its projections (*16*). The image is a map on a plane of different signal intensities, coming from the observed paramagnetic agent.

Since the EPR spectrum is a function of the EPR signal against the magnetic field H_0, imaging is performed by adding a linear field gradient, $H(r) = G \cdot r$, to the stationary magnetic field, H_0, required to observe the magnetic resonance phenomenon (*17*).

The EPR spectrum of an object recorded in the presence of a field gradient along a direction r represents the projection $p_\phi(r)$ on r of the sample spin density and is given by

$$s(H) = \int_{-\infty}^{\infty} p(z - H)t(H)dz. \qquad [8]$$

The function $t(H)$ represents the lineshape function and corresponds to the EPR spectrum measured in the absence of a field gradient; $p(H)$ describes the spatial distribution of the

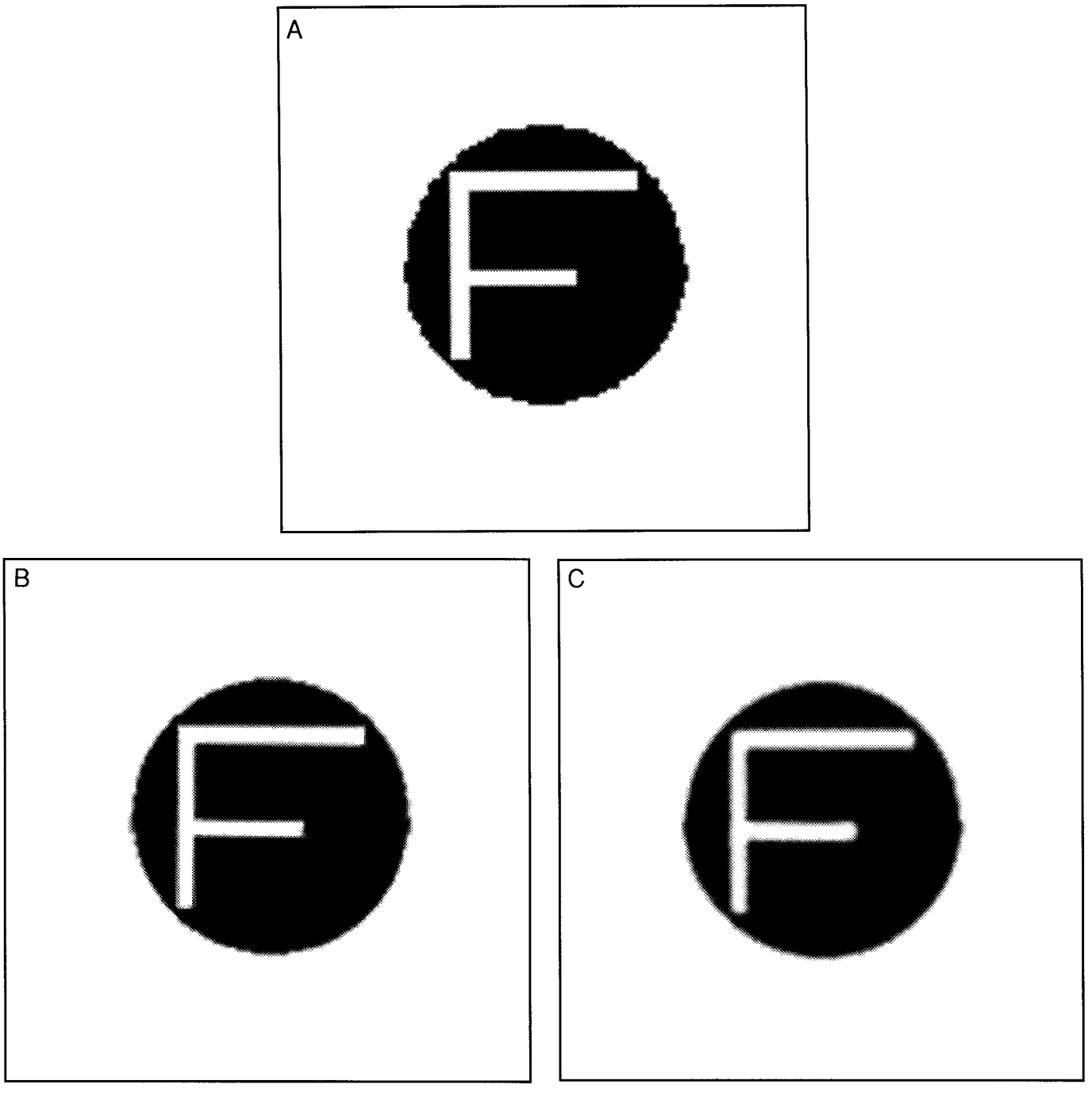

FIG. 1. Two-level sample image (A) composed of an "F" printed on a white cylinder. The maximum value of the image, white, corresponds to 1; the minimum value, black, corresponds to 0. Correct Fourier reconstruction (B), 128*128, and filtered back projection reconstruction (C), 128*128, of the sample image shown in (A). The set of projections used to obtain the images (B) and (C) was composed of 128 projections, each sampled on 128 points.

spin density. This expression means that the signal measured in the presence of a field gradient is the convolution of the intrinsic linewidth of the studied species with the spatial distribution of the sample.

In the case of SSI, the purpose is not only to obtain the spin density information, but also to differentiate the spectral information from localized parts of the sample.

The image obtained by a 2D SSI experiment, in fact, represents the spread of EPR spectra along a spatial direction. The output of a SSI experiment shows a pseudo object

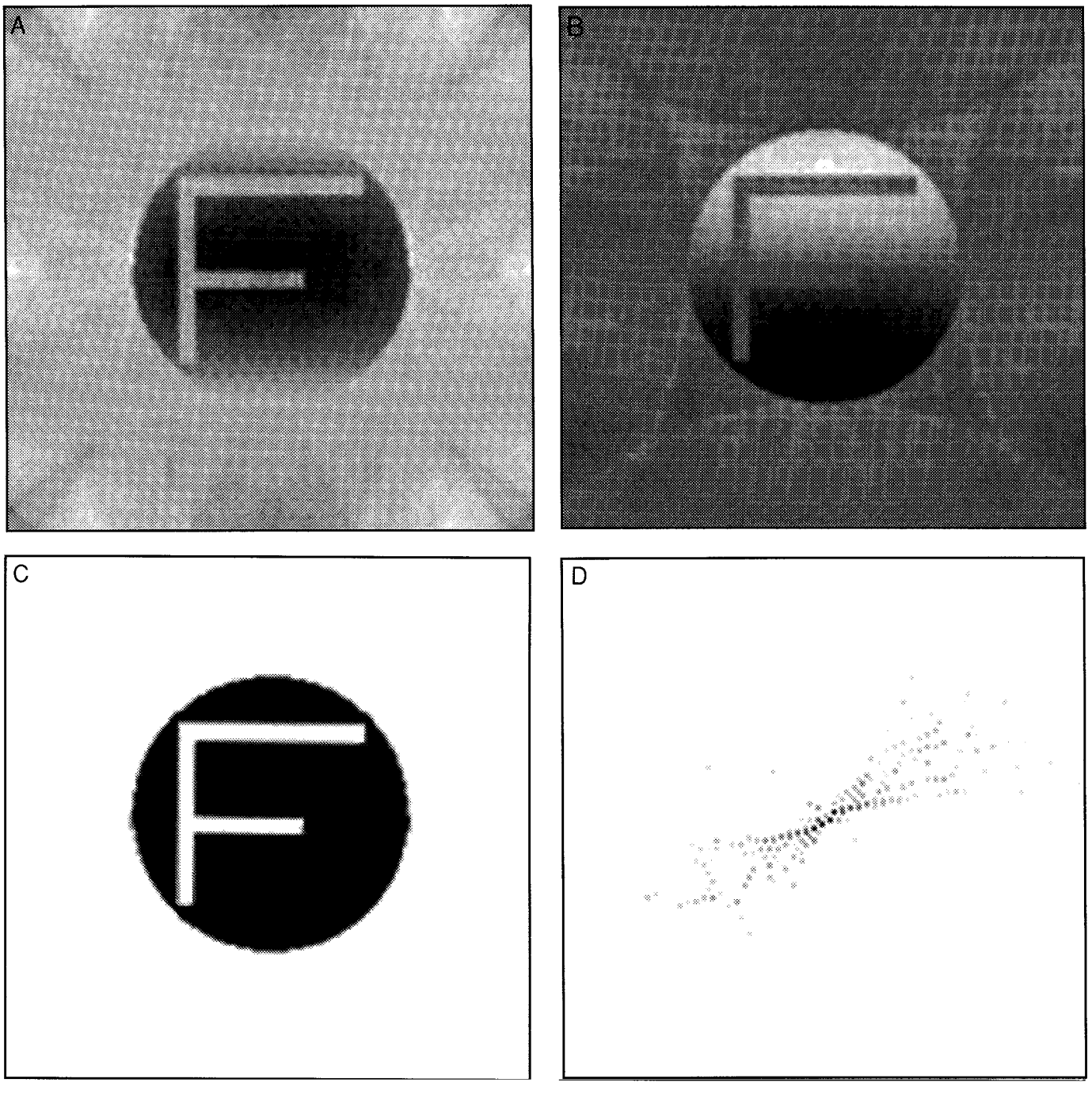

FIG. 2. Fourier reconstruction, 128*128, of the sample image shown in Fig. 1A. Real part (A) and imaginary part (B) of the reconstruction with one-point shift of the Fourier transform of one projection. Real part (C) and imaginary part (D) of the reconstruction with correct positioning of the Fourier coefficients of all the projections. The image shown in (C) is the same as that reported in Fig. 1B.

whose dimensions are ΔH along the spectral axis and ΔS along the spatial axis. In the *H–S* plane, the lines parallel to the *H*-axis give the spectra at different positions along the sample and the spin density of the sample is represented by lines parallel to *S*. The acquisition of the EPR spectrum of an object, at a given value of the field gradient *G*, represents a projection of the pseudo object from an angle α. A field gradient equal to zero will correspond to $\alpha = 0°$ and an infinite value of the field gradient to $\alpha = 90°$. Negative values of α are obtained by inverting the gradient sign. The condition $\alpha = 90°$ is experimentally impossible to achieve because of the impossibility of using an infinitely large

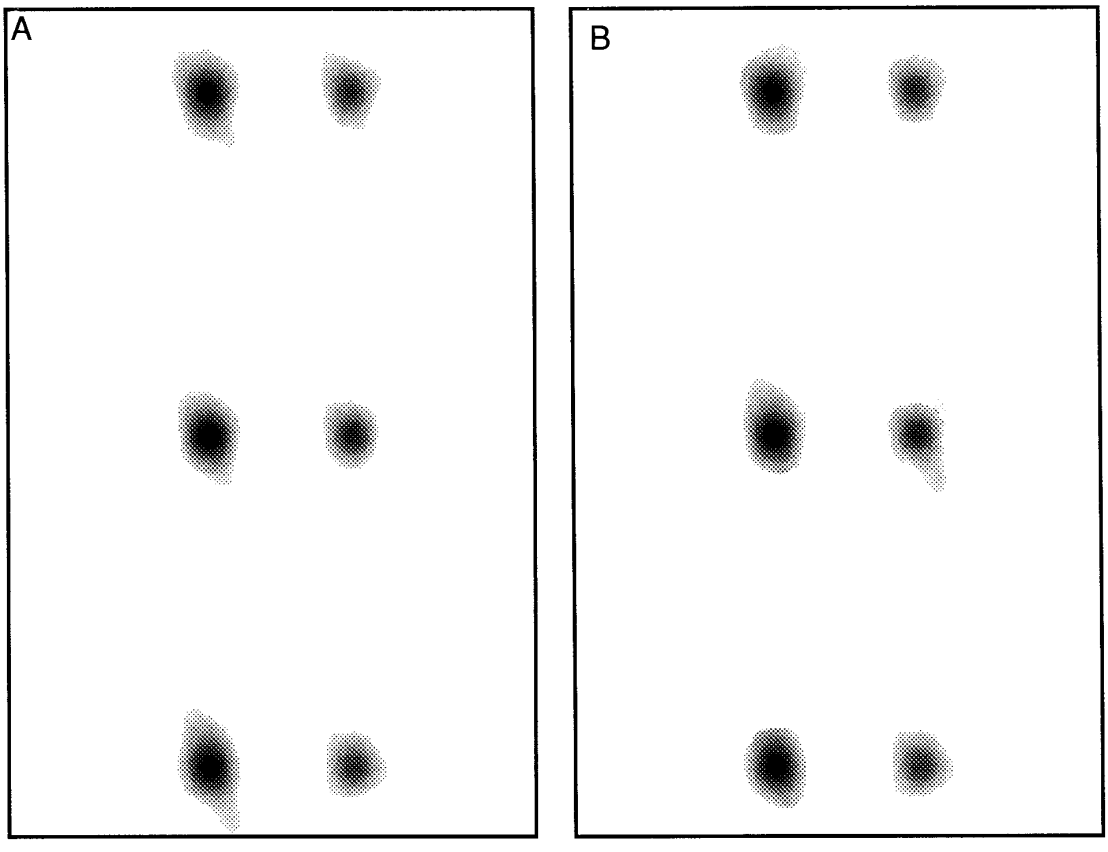

FIG. 3. L-band Fourier (A) and filtered back projection (B) spectral–spatial images of a sample composed of two contiguous circular sample holders, 4.8 and 4.3 mm in diameter and 10 mm apart. The samples were filled with a nitroxide free-radical water solution in different concentrations, 1 mM the larger and 0.7 mM the smaller. The nitroxide had the typical three-line spectrum and 0.16 mT of linewidth. To obtain the images, 33 measured projections, 4 missing angles, and 3 iterations of the algorithm were used. The maximum gradient value was 0.285 T/m.

gradient value. The relation between field gradient and observation angle α is given by

$$G_\alpha = \tan(\alpha)\Delta H/\Delta S. \quad [9]$$

The maximum observation angle α_{max} is then fixed by ΔH, ΔS and by the maximum achievable gradient intensity G_{max}. This means that an interpolating method is necessary to estimate the missing projections (due to the restricted α_{max} value). This is possible using an iterative method (*5*).

The implementation of 2D spectral–spatial that uses FR can be summarized as follows:

1. The projections are acquired at increasing gradient angles up to the maximum allowed.
2. The initial values of the missing projections are set equal to zero.
3. A Fourier reconstruction image is obtained.
4. The negative parts of the reconstructed image are set equal to zero.
5. A new estimate of the missing projections is evaluated by reprojection, at the appropriate angles, from the previous image.
6. Steps 3, 4, and 5 are repeated until there is no further improvement in the image.

It is necessary to use step 4 because if we do not make use of any constraint to change the image structure, the application of step 5 obviously gives a constant value at missing angles. This type of information would not be useful in reducing the artifacts from an image using the iterative process. In fact, a projection that gives a constant contribution to the reconstruction of an image has the same effect as a projection that is zero everywhere. Moreover, if we do not make use of any constraint to change the image structure, after the first iteration of the spectral–spatial algorithm the reprojection process would give no change in future iterations at the missing angle projections. The preceding algorithm is different from that given by Maltempo *et al.* (*5*) because step 3 is implemented using FR instead of FBP.

To show the equivalence of the two algorithms on experimental data, we reconstructed L-band (1 GHz) EPR spectral–spatial FR and FBP images of a phantom composed of two

contiguous circular sample holders, 4.8 mm and 4.3 mm in diameter and 10 mm apart. The sample holders were filled with a nitroxide free-radical water solution in different concentrations, 1 mM the larger and 0.7 mM the smaller. The free radical used had the typical three-line spectrum of nitroxides and 0.16 mT of linewidth. To obtain the spectral–spatial images using the two techniques we used 33 measured projections, 4 missing angles, and a maximum gradient value $G_{\max}$ of 0.285 T/m. The optimal number of iterations was 3 for both algorithms. The images obtained with FR and FBP are shown in Figs. 3A and 3B, respectively. The images are the visualization of the nitroxide free-radical triplet, reproduced twice (one for each sample tube) with different intensities, due to the different concentrations of the solutions. The two images show that very similar results are obtained by using the two techniques.

The experimental projections were collected at different gradient values and the projections have different S/N values. The signal-to-noise ratio (S/N) of the experimental projections was calculated as the ratio between the signal amplitude and the standard deviation of the noise, on the integral of the projections (*18*). The maximum S/N, referred to the projection without gradient, was about 980 and the minimum S/N, calculated on the projection with maximum gradient of 0.285 T/m, was about 35. We have also calculated the S/N of the two images (image peak amplitude/standard deviation of noise) reported in Fig. 3. The FR image has a S/N of 46 and the FBP image has a S/N of 45. These results demonstrate that both techniques are equally influenced by the noise present on the data, as expected from their theoretical equivalence. Moreover, for both algorithms three iterations were necessary to obtain very similar spectral–spatial images. This fact indicates that both techniques are also equally influenced by the missing-angle artifacts.

DISCUSSION

In this paper we have shown the practical equivalence between FR and FBP. In fact, the numerical experiment demonstrates that the results obtained by the two methods are very similar if any source of phase error is removed by FR. In fact, it is important to avoid phase errors in order to have the opportunity of using FR in missing-angle applications, as in any situation in which the nonnegativity constraint and an iterative application of the reconstruction algorithm are required.

In these cases, the application of FR is recommended, because of its computational efficiency. The functionality of FR has been demonstrated when applied to spectral–spatial EPR imaging reconstruction. In this case, the iterative version of FR has been used, and the image reported in Fig. 3 demonstrates its functionality.

REFERENCES

1. R. A. Brooks and G. Di Chiro, *Phys. Med. Biol.* **21,** 689 (1976).
2. A. K. Louis and F. Natterer, *Proc. IEEE* **71,** 379 (1983).
3. F. Natterer, "The Mathematics of Computerized Tomography," p. 102, Wiley, New York (1986).
4. M. M. Maltempo, S. S. Eaton, and G. R. Eaton, in "EPR imaging and *in vivo* EPR" (G. R. Eaton, S. S. Eaton, and K. Ohno, Eds.), p. 135, CRC Press, Boca Raton, FL (1991).
5. M. M. Maltempo, S. S. Eaton, and G. R. Eaton, in "EPR imaging and *in vivo* EPR" (G. R. Eaton, S. S. Eaton, and K. Ohno, Eds.), p. 145, CRC Press, Boca Raton, FL (1991).
6. A. Sotgiu, G. Placidi, G. Gualtieri, C. Tatone, and C. Campanella, *Magn. Res. Chem.* **33,** 160 (1995).
7. G. Placidi, Ph.D. thesis, University of L'Aquila (1996).
8. S. Colacicchi, M. Alecci, G. Gualtieri, V. Quaresima, C. L. Ursini, M. Ferrari, and A. Sotgiu, *J. Chem. Soc. Perkin Trans. 2, 2077 (1993).*
9. E. O. Brigham, "The Fast Fourier Transform," p. 184, Prentice Hall, New York (1974).
10. P. F. C. Gilbert, *Proc. Roy. Soc. Ser. B* **182,** 89 (1972).
11. D. G. Grant, *IEEE Trans. Bio-Med. Eng.* **19,** 20 (1972).
12. C. M. Lai, *J. Appl. Phys.* **52,** 1141 (1981).
13. A. Rosenfeld and A. C. Kak, "Digital Picture Processing," Vol. 1, p. 353, Academic Press, New York (1982).
14. R. M. Mersereau and A. V. Oppenheim, *Proc. IEEE* **62,** 1319 (1974).
15. G. Placidi, M. Alecci, and A. Sotgiu, *J. Magn. Reson. B* **108,** 50 (1995).
16. M. Alecci, M. Ferrari, V. Quaresima, A. Sotgiu, and C. L. Ursini, *Biophys. J.* **67,** 1274 (1994).
17. K. Ohno, G. R. Eaton, and S. S. Eaton, Eds., "EPR Imaging and *in Vivo* EPR," p. 3, CRC Press, Boca Raton; FL (1991).
18. R. R. Ernst, *in* "Advances in Magnetic Resonance," (J. S. Waugh, Ed.), p. 1, Academic Press, New York (1966).